

Are complex magnetic field structures responsible for the confined X-class flares in super active region 12192?

Jun Zhang, Ting Li, Huadong Chen

ABSTRACT

From 2014 October 19 to 27, six X-class flares occurred in super active region (AR) 12192. They were all confined flares and were not followed by coronal mass ejections (CMEs). To examine the structures of the four flares close to the solar disk center from October 22 to 26, we employ firstly composite triple-time images in each flare process to display the stratified structure of these flare loops. The loop structures of each flare in both lower (171 Å) and higher (131 Å) temperature channels are complex, e.g., the flare loops rooting at flare ribbons are sheared or twisted (enwound) together, and the complex structures have not been destroyed during the flares. For the first flare, although the flare loop system appears as a spindle shape, we can estimate their structure from observations, with lengths ranging from 130 to 300 Mm, heights from 65 to 150 Mm, widths at the middle part of the spindle from 40 to 100 Mm, and shear angles from 16° to 90°. Moreover, the flare ribbons display irregular movements, such as the left ribbon fragments of the flare on 22 swept a small region repeatedly, and the both ribbons of the flare on 26 moved along the same direction, instead of separating from each other. These irregular movements also imply that the corresponding flare loops are complex, e.g. several sets of flare loops are twisted together. Although previous studies suggest that the background magnetic fields prevent confined flares from erupting, we firstly suggest based on these observations that the complex flare loop structures may be responsible for these confined flares.

Subject headings: Sun: activity — Sun: atmosphere — Sun: corona — magnetic reconnection

Key Laboratory of Solar Activity, National Astronomical Observatories, Chinese Academy of Sciences, Beijing 100012, China; zjun@nao.cas.cn; hdchen@nao.cas.cn. University of Chinese Academy of Sciences, Beijing 100049, China

1. Introduction

The flares associated with coronal mass ejections (CMEs) are termed “eruptive flares” and the eruptive flares usually last for a long period, from tens of minutes to hours (e.g., Zhang et al. 2007). Some flares are not accompanied by CMEs in the wake of the eruption (Ji et al. 2003), these flares are called confined flares (e.g., Wang & Zhang 2007). The occurrence rate of eruptive flares is dependent on the flare intensity and duration (Kahler et al. 1989; Andrews 2003). The fraction of flares that is associated with CMEs increases rapidly as go from small flares to large X-class flares, reaching close to 100% for the largest ones. For example, Yashiro et al. (2005) find that the fraction of flares associated with CMEs increases from 20% for C3–C9 flares to 100% for flares above X3. Wang & Zhang (2007) reported whether a flare is eruptive or confined is determined by the distance between the flares and the active regions, such as 22–37 Mm for eruptive flares and 6–17 Mm for confined flares. On the other hand, the overlying magnetic arcades provide strong confinement, and are believed to play an important role in the failed eruptions (e.g., Török & Kliem 2005; Guo et al. 2010; Cheng et al. 2011; Chen et al. 2013).

To explain the physical mechanism of eruptive events, many theories and models have been proposed, in which the overlying magnetic loops should be opened so that plasma and magnetic flux can escape (Forbes et al. 2006). For the eruptive flares, a rising flux rope stretches the overlying magnetic lines, then a magnetic reconnection between the stretching lines takes place (Sturrock 1966; Masuda et al. 1994; Shibata et al. 1995; Tsuneta 1996). The confined flares are mainly affected by the surrounding coronal magnetic fields. Török & Kliem (2005) and Fan & Gibson (2007) revealed that while the overlying arcade field decreases slowly with height, a confined event is permitted. Furthermore, the calculations from the potential field source-surface model showed that stronger overlying magnetic arcades will prevent energy release, thus resulting in confined flares (Wang & Zhang 2007; Guo et al. 2010; Chen et al. 2015).

A large number of simulations about the question whether a configuration fully or partly erupts have been investigated. Examining the magnetohydrodynamic (MHD) stability, analyzing nonlinear force-free field (NLFFF) models, and employing the techniques of flux rope insertion (van Ballegooijen 2004; van Ballegooijen et al. 2007) and magnetofrictional relaxation (Yang et al. 1986), Kliem et al. (2013) confirmed that the MHD treatment of the eruptive configuration can reappear some observed features. Considering the condition that a toroidal flux rope embeds in a bipolar or quadrupolar external field, catastrophe and torus instability occur at an X-line under the flux rope where magnetic reconnection takes place (Kliem et al. 2014a). Through studying force-free equilibria containing two vertically arranged magnetic flux ropes (Titov & Demoulin 1999; Liu et al. 2012), Kliem et al. (2014b)

have demonstrated several conditions for the two ropes activities, e.g. both the ropes turn unstable, both the ropes erupt upward, and only the upper rope erupts while the lower rope reconnects with the ambient flux.

In this work, we report four confined X-class flares by analyzing the complex flare loops, with the observations from the Atmospheric Imaging Assembly (AIA; Lemen et al. 2012) and the Helioseismic and Magnetic Imager (HMI; Scherrer et al. 2012; Schou et al. 2012) aboard the *Solar Dynamics Observatory* (SDO; Pesnell et al. 2012). The data from the *Interface Region Imaging Spectrograph* (IRIS; De Pontieu et al. 2014) are also employed to display the special evolution of these flare ribbons. In Section 2, we describe the observational data. The results are presented in Section 3. Section 4 displays the conclusions and a brief discussion.

2. Observations

SDO/AIA observes the Sun in ten wavelengths with a $0''.6$ pixel size and a 12 s cadence. These data reveal the solar atmospheric temperatures from ~ 5000 K to ~ 20 MK. The SDO/HMI records the full disk line-of-sight (LOS) magnetic field with a cadence of 45 s and a spatial sampling of $0''.5$ pixel $^{-1}$. We use the observations of 131, 171 and 1600 Å to investigate the evolutions of flare loops and ribbons, and the LOS magnetograms are applied to display the photospheric magnetic fields of these loops. The data adopted here were obtained from 2014 October 22 to 26 while AR 12192 was near the solar disk center. We have de-rotated the AIA data to the same time (October 23 15:00 UT). Furthermore, two sets of IRIS 1330 Å data are employed. The first set of IRIS observations was taken from 08:18 UT to 18:07 UT on October 22, with a cadence of 33 s, a pixel scale of $0''.16$, and a field of view (FOV) of $120'' \times 119''$. The second was taken from 23:01 UT on October 25 to 11:15 UT on October 26, with the same pixel scale and FOV of the first set, but the cadence is 18 s. The 1330 Å channel contains emission from the strong C II 1334/1335 Å lines that are formed in the upper chromosphere and transition region. In order to compare the Doppler shifts between the confined flare on October 26 and an eruptive one, we select a set of IRIS data for the eruptive X-class flare on September 10, 2014. These IRIS observations were taken from 11:28 UT to 17:58 UT, with a FOV covering the majority of the AR 12158 (Li & Zhang 2015).

3. Results

3.1. Overview of AR 12192

Due to hosting the largest sunspot group since 1990, AR 12192 observed in 2014 October has been paid significant attention (e.g., Sun et al. 2015; Thalmann et al. 2015). According to the statistics by Chen et al. (2015), while AR 12192 passed across the visible solar disk from October 18 to 29, it produced 6 X-class and 29 M-class flares. However, only one M-flare related to a CME (Li et al. 2015). These X-class flares had a similar origin within the AR and common spatial and timing characters, implying they were homologous flares (e.g., Zhang & Wang 2002; Sui et al. 2004; Yang et al. 2014), and Chen et al. (2015) suggested that tether-cutting reconnection (Moore et al. 2001) trigger these homologous flares. Thalmann et al. (2015) provided evidence for repeated energy release, indicating that the same magnetic field structures were repeatedly involved in magnetic reconnection. Sun et al. (2015) studied the magnetic conditions of the AR and suggested that the magnetic non-potentiality over the restriction of background field limited the eruptions. Photospheric motions of emerged magnetic fluxes lead to shearing the associated coronal magnetic field, which then yields a tether-cutting favorable configuration (Chen et al. 2015).

3.2. Complex flare loops

One outstanding feature of AR 12192 is its poor CME production rate, despite many X-class flares observed during its disk passage. Previous studies suggested that the overlying background field of the AR may play an important role in these confined flares. In this work, we focus on the complex flare loops themselves. Four X-class flares (from October 22, 2014 to October 26, 2014) which occurred close to the solar disk center are studied. Figure 1 display the loops of the first studied X-class flare (X1 in Fig. 1a) on October 22, 2014. During the flare process, the flare loops at higher temperature (e.g. 131 Å, Figs. 1d-1f, see also the online animated version of Figure 1) were more abundant than those at lower temperature (171 Å, Figs. 1a and 1b). These loops displayed complex structures, such as the loops which are sheared relative to each other in Fig. 1e, and rooted at two flare ribbons which were more evident at 171 Å (Fig. 1a) and 1600 Å (Fig. 1c). From the corresponding LOS magnetogram (Fig. 1g), we notice that the left ribbon overlaps the negative polarity fields, and the right ribbon positive fields.

To better show these flare loops, we employ for the first time composite triple-time images of 131 Å observations which can clearly display the complex loops during flare processes. Composite triple-filter images (e.g. Zhang et al. 2015) from SDO/AIA are widely used to

display the different temperature structures in the solar atmosphere. The composite triple-time images are derived from the hint of composite triple-filter images, and are produced by imitating the composite triple-filter images. The imitation is based on the observational fact that the flare loops brighten successively from lower to higher atmospheric levels in the flare process. In other words, each set of flare loops seems immobile during the flare process. While we display these successively brightened loops with different colours in ONE image, stratified structure of these flare loops appears. For example, in Fig. 1h, the blue loops are lower and shorter, yellow loops are located at the middle layer, and the red loops are higher and longer, and are located at the highest layer. The majority of the flare loops rooted at a small region on the left, but on the right the loops rooted at a long extending ribbon, thus appearing a spindle structure (see Figs. 1c and 1h). The lengths of flare loops can be reliably measured. Assuming that the loops are semicircular configurations, so the corresponding height (equals the half of the length) can be determined also. To describe the properties of these loops, the lengths, heights (widths) of particular loops (loop systems) of the first flare, the lengths and heights of the other three flare loops are listed in Table 1. Certainly the assumption may not be well justified in complex active regions, as the loops have a more complicated geometry far away from circular. The heights of loops in each flare are for references only. To quantitatively describe the complexity of the flare loops, shear angles in the first two flares are measured by comparing the observed loops with the AR’s prime neutral lines deduced from the magnetograms. The flare loops are higher non-potential, e.g. strong shear (or deviating from potential fields) in 131 Å images. The shear angles of X1 loops distribute from 16° to 90° (see Table 1).

Figure 3 shows the loops of the second studied X-class flare (X2 in Fig. 3a) on October 24, 2014. Similar to the first flare displayed in Figure 1, this flare shown also complex loop structures. The twisted loops were observed in lower (171 Å, Figs. 3b and 3c) temperature wavelength, and the shear angles are estimated from 30° to 85° (see Fig. 3h and Table 1). The last two X-class flares, which occurred on October 25 and 26 respectively, were displayed

Table 1. Spatial scales and shear angles of the flare loops (loop systems) in X1–X4

Parameter	X1	X2	X3	X4
<i>Length</i> (Mm)	130 – 300	173 – 480	214 – 420	150 – 400
<i>Height</i> (Mm)	65 – 150	86 – 240	107 – 210	75 – 200
<i>Width</i> (Mm)	40 – 100			
<i>Shear angles</i> (°)	16 – 90	30 – 85		

in Figure 4. Also these flare loops were non-potential, and the shear of the loops was evident (see Fig. 4b and the window region of Fig. 4f). As the third and fourth flares were near the solar limb, the widths and the shear angles of flare loop systems can not be reliably measured. During all the four X-class flare processes, the complex structures had not been destroyed. Also the signal for the open and shrink of these flare loops was not evident.

3.3. Special evolution of flare ribbons

Previous studies for these flares have realized the large initial separation of these flare ribbons, together with an almost absent growth in ribbon separation, suggests a confined reconnection site high up in the corona. Two sets of *IRIS* 1330 Å data with high spatial resolution allow us to investigate the detail evolution of the ribbons of the first and the fourth flares. Figure 2 is time series of the first set of *IRIS* 1330 Å images (also see the online animated version of Figure 2) which show the evolution of four fragments (marked by “R1”, “R2”, “R3”, and “R4”, respectively) of the flare “X1” ribbons (see Fig. 1). “R1” which belongs to the right ribbon and appears as a hook propagates leftward. The moving speed of “R1” has been deduced by examining the evolution of the ribbons observed from *IRIS* images. As the spatial resolution of the *IRIS* data is much high ($0''.16$ per pixel), and the moving process lasted a long time (13.5 min, see Figs. 2a and 2e), the speed error is small. Considering the position error is 2 pixels while we measure the speeds, the speed error is 0.6 km s^{-1} , so the propagating speed is $19 \pm 0.6 \text{ km s}^{-1}$ (Fig. 2e). The three fragments “R2”, “R3”, and “R4” belong to the left ribbon of the flare. They appear successively, and sweep repeatedly a small region anticlockwise. Another evolution pattern of flare ribbons revealed by the second set of *IRIS* 1330 Å data is both of the two ribbons move along the same direction, instead of separating from each other. Figures 5a and 5b show the evolution of two ribbons of the fourth flare (X4) in the field-of-view outlined in Fig. 4f. Both the ribbons move rightward, with a speed of $11 \pm 0.5 \text{ km s}^{-1}$ ($19 \pm 0.5 \text{ km s}^{-1}$) for the left (right) ribbon (see Fig. 5c).

3.4. Different Doppler shifts between a confined flare and an eruptive one

As there is no material escape from the solar atmosphere in a confined flare process, the Doppler shifts between a confined flare and an eruptive one will be different. We compare the confined flare (X4) on 2014 October 26 with the eruptive one on 2014 September 10. Figure 5d shows the variation of the GOES soft X-ray flux (blue curve) in the X4 flare duration. The black cross symbols show the Doppler shifts in the position (denoted by a yellow cross

symbol in Fig. 5b) which locates at the middle region of the two flare ribbons. The redshift velocities ($10\text{--}30\text{ km s}^{-1}$) are almost stable during the flare process. Furthermore, Figs. 4e-4h have already showed that these flare loops are restricted to a limited region. For the flare with mass ejection on 2014 Sep. 10, we can not plot truly the heights of the flare loops above the photosphere where the Doppler velocity has been measured, as the loops at the position rise almost along the line-of-sight. Fortunately we can track the loops which cross over the position (where the Doppler velocity has been measured) from one footpoint to another one, so the relative height of the loop at other position can be truly measured (see Figs. 5e–5g). Near 17:25 UT on 2014 Sep. 10, the projective height of the loops reached 100 Mm, and the rising speed exceeded 200 km s^{-1} . Moreover, the eruptive X-class flare displayed different Doppler shifts, e.g. at the later phase of the flare, the redshift velocities in the middle of the two ribbons increased from 30 km s^{-1} to about $80\text{--}100\text{ km s}^{-1}$ (Fig. 5h, see Li & Zhang 2015).

4. Conclusions and Discussion

Examining the evolution of the four flares from October 22 to 26, we note that the loop structures of each flare in both lower (171 \AA) and higher (131 \AA) temperature channels were complex, e.g., the flare loops rooting at flare ribbons were twisted (enwound) together, strong shear among loops and evidently non-potential features of the flare loops. *IRIS* observations display that the flare ribbons underwent irregular movement, such as the left ribbon of the flare on 22 swept repeatedly a small region, and the both ribbons of the flare on 26 moved along the same direction, instead of separating from each other. By comparing the confined flare X4 with the eruptive one on 2014 September 10, we find that the eruptive flare displayed a strong Doppler redshift enhancement and the rising speed of the flare loops reached 200 km s^{-1} at the late phase of the flare, but no redshift enhancement for the confined one, implying that the complex flare loops did not open and then shrink. Based on these observations, we firstly suggest that the complex flare structures tie themselves up, and there is no enough energy to untangle these fastened structures, so these flares are observed as confined ones.

In previous studies, the dominant idea to interpret confined flares is the overlying loops preventing the flares from being eruptive. Indeed there are some large-scale coronal loops above confined flares are observed (Yang et al. 2014). However, the complex flare loops may also play a key role, but it is always omitted. In fact, observations reveal that there are many loops involved in a flare, and these loops will erupt if the flare is an eruptive one. Under the condition that these eruptive loops are individual, e.g. potential field loops, the overlying loops should cover fully all these individual flare loops to prevent them from erupting. So we

should observe a network (or a dome) which consists by the overlying loops enwrapping the flare loops. On the contrary, only one or two sets of overlying loops (arcades) are detected during confined flare processes (Chen et al. 2013, Yang et al. 2014). These evidences suggest that the flare loops are not individual, instead, they are enwound together, so one or two set of overlying loops can prevent them from erupting. Our observations supporting that the loops of each studied flare are indeed enwound together. Liu et al. (2014) reported a confined flare with a quasi-static cusp-shaped structure which consists of multiple nested loops, implying that the flare loops are also enwound together.

Another evidence to display the complex flare loops is the evolution of flare ribbons. The flare ribbons are considered as mapping the energy release site in solar flares. The movement of the ribbons and its relationship to magnetic fields are important for understanding the magnetic reconnection process. The two ribbons in many flares appear to separate from each other during the developing process of the flares (e.g., Fletcher & Hudson 2002; Qiu et al. 2002; Asai et al. 2004; Veronig et al. 2006; Miklenic et al. 2007; Temmer et al. 2007; Li & Zhang 2009). In our studied events, the two ribbons of each flare are evident, but the separation of the two ribbons is absent. Furthermore, the detail observations from *IRIS* display that the ribbons undergo special evolution. For the first studied flare, the ribbon fragments (see Fig. 2) “R2”, “R3” and “R4” swept successively a small region along different directions, indicating that the corresponding flare loops are enwound together. AIA observations confirm that the flare loops are enwound, e.g. shear each other in Fig. 1e. For the fourth flare, the two ribbons move along the same direction (Figs. 5a and 5b) with speeds of 10 to 20 km s⁻¹, instead of separation. We can imagine that only braiding flare loops can produce the two ribbons moving along the same direction, and the AIA observations (shear loops in Fig. 4) support the scenario.

During the fourth flare process, the redshift velocities (10–30 km s⁻¹) at the middle region of the two ribbon are almost stable, suggesting that there is no violent upward (downward) movement enhancement in the lower atmosphere. In other words, the complex magnetic structures relevant to the flare do not undergo ascending (descending) process, or the complex magnetic structures are stable and do not affect by the flare. For comparison, the eruptive X-class flare on 2014 September 10 displayed different Doppler shifts, e.g. at the later phase of the flare, the redshift velocities at post-flare loop position increased from 30 km s⁻¹ to about 80–100 km s⁻¹ (Fig. 5h) in the transition region (Li & Zhang 2015), implying the violent downward-moving cool and dense chromospheric and transition region condensations (Fisher et al. 1985) during the gradual phase. This study is only a preliminary step to investigate the complex magnetic structures for confinement of solar flares. To further evaluate the effectiveness of these complex structures, a more robust study involving more events is needed.

This work is supported by the National Natural Science Foundations of China (11533008 and 11673034). The data are used courtesy of NASA/*SDO* and *IRIS* science teams.

REFERENCES

- Andrews, M. D. 2003, *Sol. Phys.*, 218, 261
- Asai, A., Yokoyama, T., Shimojo, M., et al. 2004, *ApJ*, 611, 557
- Chen, H., Ma, S., & Zhang, J. 2013, *ApJ*, 778, 70
- Chen, H., Zhang, J., Ma, S., et al. 2015, *ApJ*, 808, L24
- Cheng, X., Zhang, J., Ding, M. D., Guo, Y., & Su, J. T. 2011, *ApJ*, 732, 87
- De Pontieu, B., Title, A. M., Lemen, J. R., et al. 2014, *Sol. Phys.*, 289, 2733
- Fan, Y., & Gibson, S. E. 2007, *ApJ*, 668, 1232
- Fisher, G. H., Canfield, R. C., & McClymont, A. N. 1985, *ApJ*, 289, 414
- Fletcher, L., & Hudson, H. S. 2002, *Sol. Phys.*, 210, 307
- Forbes, T. G., Linker, J. A., Chen, J., et al. 2006, *Space Sci. Rev.*, 123, 251
- Guo, Y., Ding, M. D., Schmieder, B., et al. 2010, *ApJ*, 725, L38
- Ji, H., Wang, H., Schmahl, E. J., Moon, Y.-J., & Jiang, Y. 2003, *ApJ*, 595, L135
- Kahler, S. W., Sheeley, N. R., Jr., & Liggett, M. 1989, *ApJ*, 344, 1026
- Kliem, B., Su, Y. N., van Ballegooijen, A. A., & DeLuca, E. E. 2013, *ApJ*, 779, 129
- Kliem, B., Lin, J., Forbes, T. G., Priest, E. R., & Török, T. 2014a, *ApJ*, 789, 46
- Kliem, B., Török, T., Titov, V. S., et al. 2014b, *ApJ*, 792, 107
- Lemen, J. R., Title, A. M., Akin, D. J., et al. 2012, *Sol. Phys.*, 275, 17
- Li, L., & Zhang, J. 2009, *ApJ*, 690, 347
- Li, T., & Zhang, J. 2015, *ApJ*, 804, L8
- Li, X., Yang, S., Chen, H., Li, T., & Zhang, J. 2015, *ApJ*, 814, L13

- Liu, R., Kliem, B., Török, T., et al. 2012, *ApJ*, 756, 59
- Liu, R., Titov, V. S., Gou, T., et al. 2014, *ApJ*, 790, 8
- Masuda, S., Kosugi, T., Hara, H., Tsuneta, S., & Ogawara, Y. 1994, *Nature*, 371, 495
- Miklenic, C. H., Veronig, A. M., Vršnak, B., & Hanslmeier, A. 2007, *A&A*, 461, 697
- Moore, R. L., Sterling, A. C., Hudson, H. S., & Lemen, J. R. 2001, *ApJ*, 552, 833
- Pesnell, W. D., Thompson, B. J., & Chamberlin, P. C. 2012, *Sol. Phys.*, 275, 3
- Qiu, J., Lee, J., Gary, D. E., & Wang, H. 2002, *ApJ*, 565, 1335
- Scherrer, P. H., Schou, J., Bush, R. I., et al. 2012, *Sol. Phys.*, 275, 207
- Schou, J., Scherrer, P. H., Bush, R. I., et al. 2012, *Sol. Phys.*, 275, 229
- Shibata, K., Masuda, S., Shimojo, M., et al. 1995, *ApJ*, 451, L83
- Sturrock, P. A. 1966, *Nature*, 211, 695
- Sui, L., Holman, G. D., & Dennis, B. R. 2004, *ApJ*, 612, 546
- Sun, X., Bobra, M. G., Hoeksema, J. T., et al. 2015, *ApJ*, 804, L28
- Temmer, M., Veronig, A. M., Vršnak, B., & Miklenic, C. 2007, *ApJ*, 654, 665
- Thalmann, J. K., Su, Y., Temmer, M., & Veronig, A. M. 2015, *ApJ*, 801, L23
- Titov, V. S., & Démoulin, P. 1999, *A&A*, 351, 707
- Török, T., & Kliem, B. 2005, *ApJ*, 630, L97
- Tsuneta, S. 1996, *ApJ*, 456, 840
- van Ballegooijen, A. A. 2004, *ApJ*, 612, 519
- van Ballegooijen, A. A., Deluca, E. E., Squires, K., & Mackay, D. H. 2007, *Journal of Atmospheric and Solar-Terrestrial Physics*, 69, 24
- Veronig, A. M., Karlický, M., Vršnak, B., et al. 2006, *A&A*, 446, 675
- Wang, Y., & Zhang, J. 2007, *ApJ*, 665, 1428
- Yang, S., Zhang, J., & Xiang, Y. 2014, *ApJ*, 793, L28

- Yang, W. H., Sturrock, P. A., & Antiochos, S. K. 1986, *ApJ*, 309, 383
- Yashiro, S., Gopalswamy, N., Akiyama, S., Michalek, G., & Howard, R. A. 2005, *Journal of Geophysical Research (Space Physics)*, 110, A12S05
- Zhang, J., Li, L., & Song, Q. 2007, *ApJ*, 662, L35
- Zhang, J., & Wang, J. 2002, *ApJ*, 566, L117
- Zhang, J., Zhang, B., Li, T., et al. 2015, *ApJ*, 799, L27

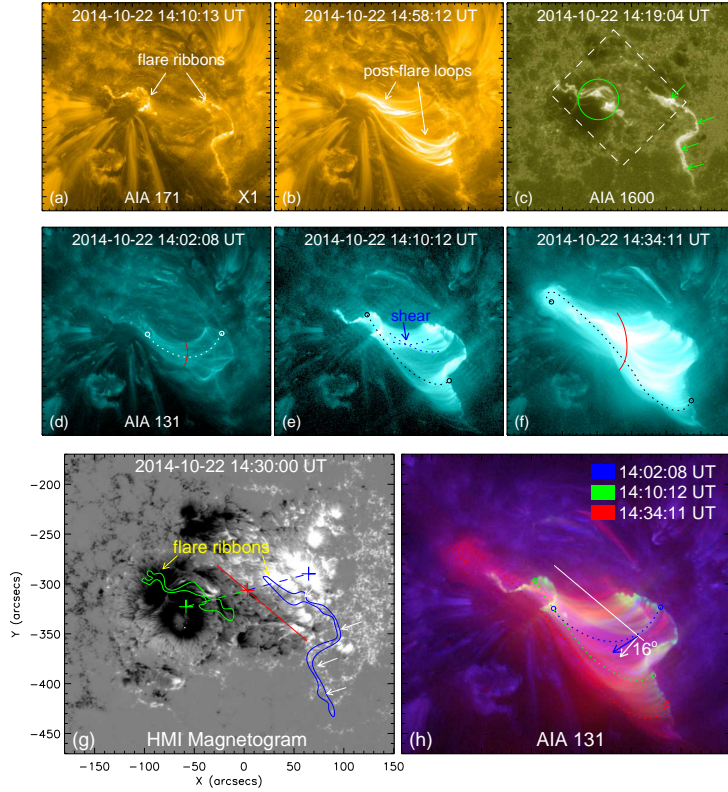


Fig. 1.— Panels (a)–(b): 171 Å images showing the flare ribbons and post flare loops of the first studied X-class flare (X1 in Fig. 1a) on October 22, 2014 at lower temperature. Panel (c): 1600 Å image displaying the two flare ribbons which are denoted by one green circle and four green arrows, respectively. The white window outlines the field-of-view (FOV) displayed in Figure 2. Panels (d)–(f): 131 Å images showing the flare loops at higher temperature (also see the online animation). White (Fig. 1d) and black (Figs. 1e and 1f) curves outline the lengths (see Table 1) of the flare loops at different times. Two red curves in Figs. 1d and 1f denote the widths of the loop systems, and two crossed blue curves in Fig. 1e show the shear of the loops. Panel (g): corresponding line-of-sight (LOS) magnetogram. The blue and green curves are the contours of the flare ribbons displaying in panel (c). The green, blue, and red pluses correspond to the locations of the maximum negative flux, maximum positive flux, and their midpoint, respectively. The red line outlines the AR prime magnetic polarity inversion line (PIL, Chen et al. 2015). Panel (h): composite triple-time images of 131 Å images consisting of 14:02 UT (blue), 14:10 UT (green), and 14:34 UT (red) images. The white line is the duplication of the PIL (the red line in Fig. 1g). The blue, yellow and red curves are the duplications of the white curve in Fig. 1d, the black curve in Fig. 1e and the black curve in Fig. 1f, respectively. The angle 16° represents the shear angle between the blue arrow (represents the tangent of the blue curve at the intersection of the blue curve and PIL) and the white arrow (the line perpendicular to the PIL). An online animated version of the 131 Å images is available. The 14s animation runs from 14:00 to 15:00 UT.

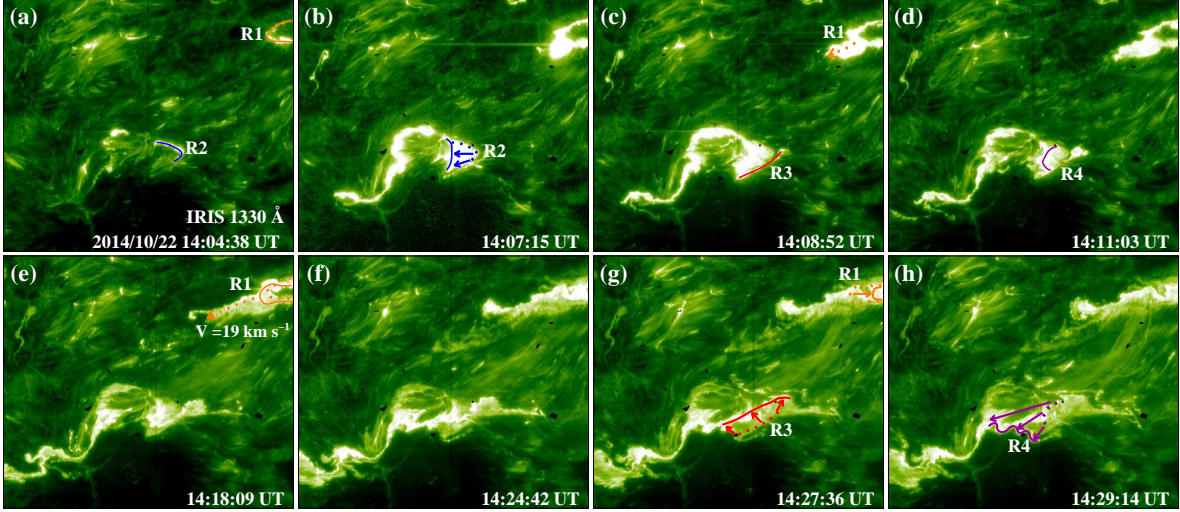


Fig. 2.— Time series of *IRIS* 1330 Å images showing the evolution of four fragments (marked by “R1”, “R2”, “R3”, and “R4”, respectively) of the two flare ribbons (see Fig. 1). Panel (a): the first appearance of “R1” (outlines by a solid yellow curve) and “R2” (outlines by a solid blue curve). Panel (b): leftward sweeping of “R2”. The blue arrows denote the sweeping direction, the blue solid curve outlines the left boundary of “R2”, and the dotted blue curve is the duplication of the blue curve in Fig. 2a. Panel (c): “R3” (outlined by a red curve) first appearance. Panel (d): “R4” (the purple curve) first appearance. The dotted yellow arrows in Figs. 2c and 2e denote the propagating direction of “R1” from the curve top of “R1”, and the solid yellow arrow in Fig. 2g the shrinking direction of “R1”. This propagation last almost twenty minutes (from 14:04 UT to 14:24 UT, see Figs. 2a–2f), with the largest propagating speed of $19 \pm 0.5 \text{ km s}^{-1}$ (see Fig. 2e). “R1” enlarges at first, and then shrinks (see the solid yellow curves in Figs. 2e and 2g). The dotted curve in Fig. 2e is the duplication of the yellow curve in Fig. 2a, and the dotted curve in Fig. 2g is the duplication of the solid curve in Fig. 2e. “R3” sweeps up-leftward (see the red curve in Fig. 2g), with the red arrows denoting the sweeping direction, and the dotted red curve the duplicate of the curve in Fig. 2c. “R4” sweeps down-leftward (see the purple curve in Fig. 2h, the arrows denote the sweeping direction). The dotted purple curve in Fig. 2h is the duplication of the curve in Fig. 2d. An online animated version of this Figure is available. The 9s animation runs from 14:00 to 15:00 UT.

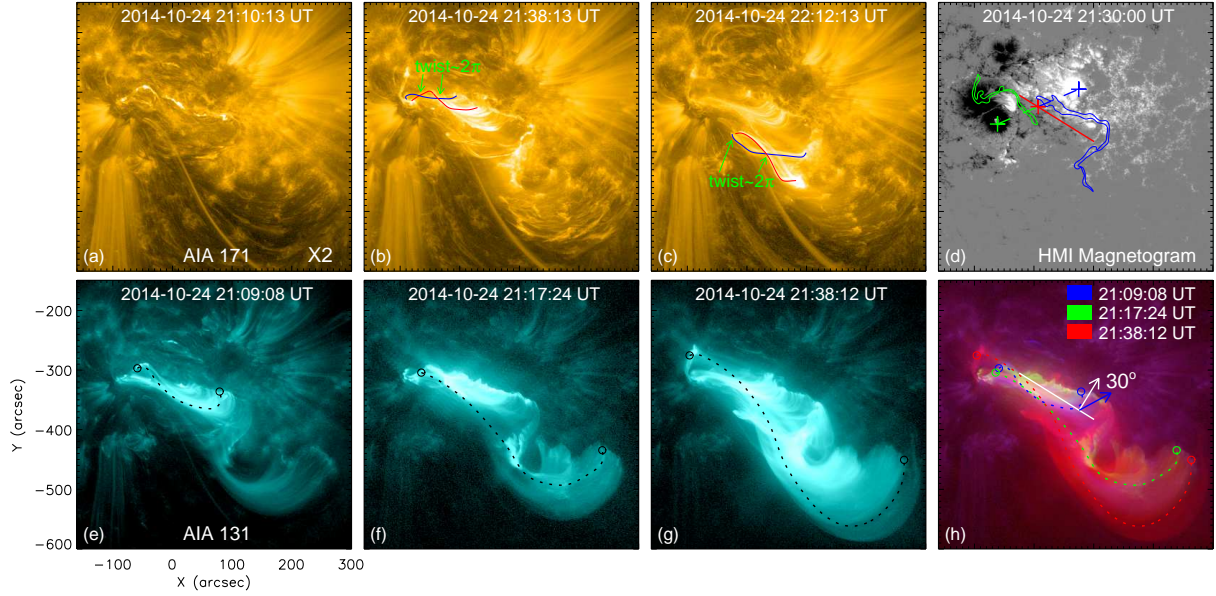


Fig. 3.— Panels (a)–(c): 171 Å images showing the loops of the second studied X-class flare (X2 in Fig. 3a) on October 24, 2014 at lower temperature. The crossed red and blue curves in Figs. 3b and 3c represent the twisted flare loops. Panel (d): corresponding LOS magnetogram. Contours, lines and pluses represent the same meanings as that in Fig. 1g. Panels (e)–(g): 131 Å images showing the loops at higher temperature. Black curves in Figs. 3e–3g outline the lengths (see Table 1) of the loops at different times. Panels (h): composite triple-time images of 131 Å images consisting of 21:09 UT (blue), 21:17 UT (green), and 21:38 UT (red) images. Curves, lines, arrows and angle represent the same meanings as that in Fig. 1h.

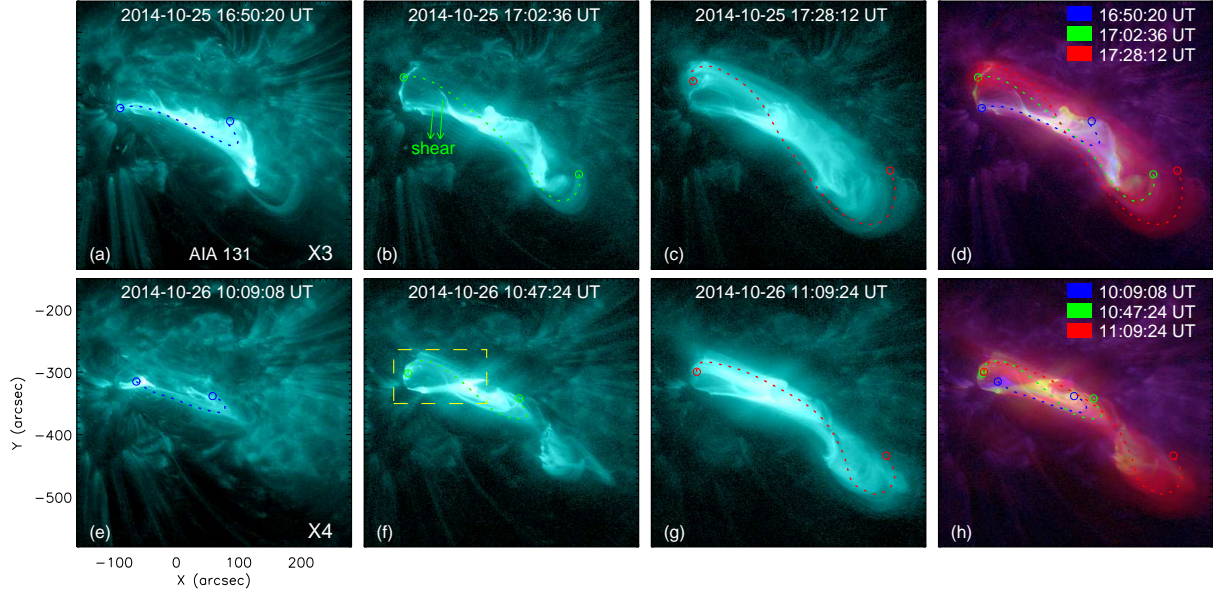


Fig. 4.— Panels (a)–(c): 131 Å images showing the loops of the third studied X-class flare (X3 in Fig. 4a) on October 25, 2014 at higher temperature. Blue, yellow and red curves outline the lengths of the loops, and are duplicated to Fig. 4d. Two yellow arrows in Fig. 4b denote the shear loops. Panel (d): composite triple-time images of 131 Å images consisting of 16:50 UT (blue), 17:02 UT (green), and 17:28 UT (red) images. Panels (e)–(g): similar to Figs. 4a–4c, 131 Å images showing the loops of the fourth studied X-class flare (X4 in Fig. 4e) on October 26, 2014. Panel (h): similar to Fig. 4d, composite triple-time images of 131 Å images consisting of 10:09 UT (blue), 10:47 UT (green), and 11:09 UT (red) images. The yellow window in Fig. 4f outlines the FOV displayed in Figs. 5a and 5b.

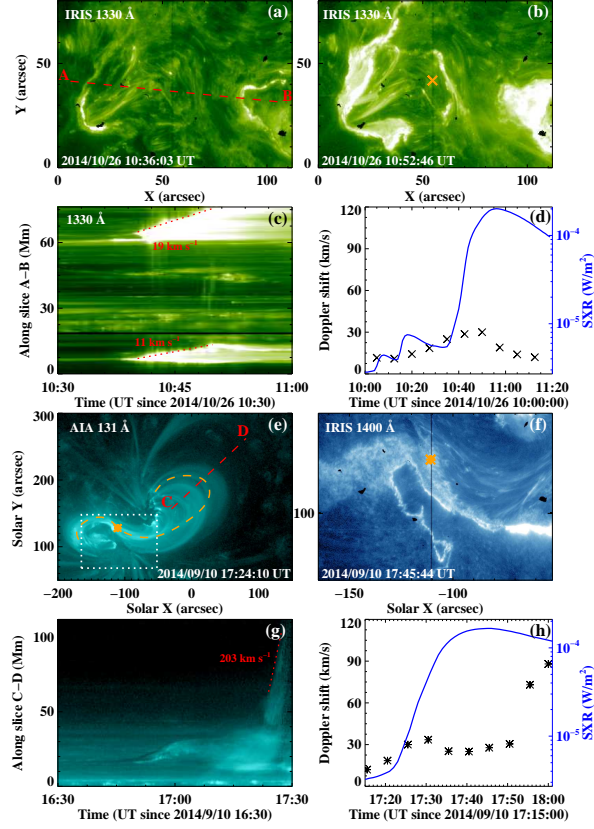


Fig. 5.— Panels (a)–(b): two *IRIS* 1330 Å images showing the evolution of two ribbons of the fourth flare (X4) in the FOV outlined in Fig. 4f. Dashed line “A-B” shows the cut position used to obtain the stack plots shown in Fig. 5c. A yellow cross symbol in Fig. 5b denotes a position where Doppler shifts are measured. Panel (d): the variation of the GOES soft X-ray flux (blue curve) in the X4 flare duration. The black cross symbols show the Doppler shifts in the position denoted in Fig. 5b. Panel (e): AIA 131 Å image showing the loops of AR 12158 on 2014 September 10. The white window outlines the FOV of Fig. 5f. A yellow star symbol denotes a position where Doppler shift are measured. Red dashed line “C-D” shows the cut position used to obtain the stack plot shown in Fig. 5g, and yellow dashed curve tracks a loop system which crosses the star symbol position. The loop system erupts afterward, with the rising speed exceeding 200 km s^{-1} . Panel (f): *IRIS* 1400 Å image showing a ribbon of the eruptive X-class flare in AR 12158. A yellow star symbol denotes the same position as the star in Fig. 5e. Panel (h): the variation of the GOES soft X-ray flux (blue curve) in the flare (on 2014 September 10) duration. The black star symbols show the Doppler shifts in the position denoted in Figs. 5e and 5f.